Iron oxides catalyze the hydrolysis of polyphosphate and precipitation of calcium phosphate minerals

Biao Wan [a], Peng Yang [b], Haesung Jung [a,c], Mengqiang Zhu [b], Julia M. Diaz [d]
Yuanzhi Tang [a,*]

[a] *School of Earth and Atmospheric Sciences, Georgia Institute of Technology, Atlanta, GA 30332-0340, United States*
[b] *Department of Ecosystem Science and Management, University of Wyoming, Laramie, Wyoming 82071, United States*
[c] *School of Civil, Environmental and Chemical Engineering, Changwon National University, Changwon, Gyeongsangnam-do, 51140, Republic of Korea*
[d] *Geosciences Research Division, Scripps Institution of Oceanography, University of California San Diego, La Jolla, CA 92093-5004, United States*

Abstract

Interfacial chemistry of phosphorus (P) is important for understanding P sequestration and bioavailability in nature. Polyphosphate is a group of important P species in aquatic environments. The geochemical behaviors of polyphosphate at the mineral-water interface play critical roles in mediating aquatic P transformation, yet remain poorly constrained. This study investigates the hydrolysis of polyphosphate in the presence of four common iron (Fe) oxide minerals (ferrihydrite, hematite, goethite, lepidocrocite) and the subsequent precipitation of calcium phosphate minerals. Batch studies are combined with microscopic and spectroscopic characterizations to reveal P speciation and complexation state under varied solution chemistry (pH 6–9, 1 mM Ca^{2+}, and artificial seawater). All four Fe oxides can hydrolyze polyphosphate and the hydrolysis rate and extent are both enhanced in the presence of Ca^{2+}. In the presence of 1 mM Ca^{2+}, the apparent hydrolysis rate fitted by first-order kinetic model follows the order of lepidocrocite > hematite > ferrihydrite > goethite. After normalization by specific surface area of Fe oxides, the hydrolysis rate is in the order of lepidocrocite ≈ goethite > hematite > ferrihydrite at pH 6, regardless of Ca^{2+} presence. At pH 7.5 and 9, the order of area-normalized apparent hydrolysis rate is lepidocrocite > goethite ≈ hematite > ferrihydrite. A terminal-only pathway via one-by-one cleavage of terminal phosphate groups is the dominant hydrolysis mechanism. Under alkaline conditions, amorphous calcium phosphate forms in the presence of Ca^{2+}, which transforms to crystalline hydroxyapatite after long-term aging of 70 or 150 days. This study demonstrates the importance of natural minerals in controlling polyphosphate transformation into crystalline calcium phosphate minerals, and provides new insights for understanding P cycling and sequestration in the environment.
© 2021 Elsevier Ltd. All rights reserved.

Keywords: Polyphosphate; Fe oxides; Hydrolysis; Apatite; Phosphorus

1. INTRODUCTION

Phosphorus (P) is an essential nutrient for all life and often viewed as a limiting macronutrient for primary production in estuarine and marine environments (Paytan and McLaughlin, 2007). Among all biological P-containing molecules, polyphosphate is an important group

* Corresponding author.
E-mail address: yuanzhi.tang@eas.gatech.edu (Y. Tang).

of phosphate-containing polymers of at least three phosphate ions joined by phosphoanhydride ($P - O - P$) bonds (Wan et al., 2019a, b). Polyphosphate widely occurs in natural systems such as soils, sediments, and aquatic environments (Omelon and Grynpas, 2008), and can be synthesized by a wide range of microorganisms such as bacteria and planktons (Diaz et al., 2008; Orchard et al., 2010; Martin et al., 2014; Zhang et al., 2015). It serves many biological functions such as being an ATP substitute, energy source, and regulator for P stress and survival, as well as for life evolution (Kornberg et al., 1999; Rao et al., 2009). It is also an important industrial chemical and is frequently used for water treatment, fertilizers, and food additives (Kulakovskaya et al., 2012), resulting in its widespread release into aquatic environments (Diaz et al., 2008; Kulakovskaya et al., 2012) and potential contamination of water bodies. Polyphosphate represents 1–13% of total P in planktonic organisms (Rao et al., 2009; Diaz and Ingall, 2010), the dissolved and particulate pools of seawater (Paytan et al., 2003; Martin et al., 2014) and marine sediments (Sannigrahi and Ingall, 2005), 1.5–11.4 % of total P in lake sediments (Hupfer et al., 2004), 0.4–7% of total P in soils (Ebuele et al., 2016), and 15–75% of total P in raw sewage and 5–40% of total P in secondary effluents of wastewater treatment systems (Guan et al., 2005; Majed et al., 2009).

In aquatic environments, especially marine settings, abundant diatom-derived polyphosphate may play key roles in geologic P sequestration and sedimentary P burial (Diaz et al., 2008). It is generally accepted that the main mechanism leading to P removal from the ocean is via the formation of apatite minerals in sediments, yet this reaction is kinetically inhibited under oceanic conditions and currently not fully understood (Diaz et al., 2008). A possible mechanism for explaining sedimentary P burial is the precipitation of fine-grained apatite mineral particles from microbially released polyphosphate intermediates (Schulz and Schulz, 2005; Diaz et al., 2008; Omelon and Grynpas, 2008; Goldhammer et al., 2010). In aquatic environments, polyphosphate transformation at the sediment–water interface was found to contribute to a significant portion of soluble reactive phosphorus, but details of the transformation process and the related formation of calcium phosphate minerals remain poorly understood (Omelon and Grynpas, 2008; Diaz et al., 2012). Our recent study on enzyme-catalyzed hydrolysis of polyphosphate indicated that orthophosphate produced from the enzymatic degradation of polyphosphate can precipitate with Ca^{2+} to form amorphous calcium phosphate (ACP) solids (Huang et al., 2018).

A few studies have explored polyphosphate transformation at the mineral-water interface and the roles of abiotic factors in controlling its stability and degradation. Triphosphate hydrolysis is facilitated by amorphous Mn oxides, and the reaction is further enhanced by the presence of Ca^{2+} and Mg^{2+} (Inman et al., 2001). Tripolyphosphate adsorption on goethite is an important step for the subsequent hydrolysis, and drying of the adsorbed tripolyphosphate in the presence of Ca^{2+} resulted in the formation of a Ca-trimetaphosphate surface complex (Hamilton et al.,

2017). However, no laboratory studies have demonstrated the formation of crystalline calcium phosphate minerals (e.g., apatite) from polyphosphate hydrolysis. We hypothesize that orthophosphate released from polyphosphate hydrolytic degradation is a key step for the nucleation and precipitation of calcium phosphate minerals. Our recent abiotic studies also showed that polyphosphate can be hydrolyzed by Al and Mn oxides, and the hydrolysis was promoted by the presence of divalent cations such as Ca^{2+} and Cu^{2+} (Wan et al., 2019a, b).

This study aims to explore the important roles of naturally abundant iron (Fe) oxide minerals in promoting polyphosphate hydrolysis and transformation under environmentally relevant conditions. Iron oxides occur ubiquitously in natural environments, with ferrihydrite, hematite, magnetite, and goethite being the most abundant; maghemite and lepidocrocite intermediately abundant; and wüstite, akaganéite, feroxyhyte, and bernalite the least abundant (Guo and Barnard, 2013). Four representative Fe oxides were used for this study, including ferrihydrite, hematite, goethite, and lepidocrocite.

Specifically, this study investigates the kinetics and mechanisms of polyphosphate adsorption and hydrolysis on these common Fe oxides under varied solution conditions including pH, presence of Ca^{2+}, and deionized (DI) water *vs* artificial seawater. For the first time of our knowledge, this study demonstrates the formation of crystalline calcium phosphate minerals (hydroxyapatite) upon aging of the reaction products. Phosphorus K-edge X-ray absorption near edge structure (XANES) spectroscopy, solution ^{31}P nuclear magnetic resonance (NMR) spectroscopy, X-ray diffraction (XRD), Fourier-transform infrared spectroscopy (FTIR), and transmission electron microscopy (TEM) with electron energy loss spectroscopy (EELS) were conducted to characterize the reaction products. Results from this study provide new insights for the abiotic transformation of polyphosphate on mineral surfaces under environmentally relevant conditions, as well as the first evidence of crystalline calcium phosphate mineral formation upon polyphosphate hydrolysis in the presence of Ca^{2+}.

2. MATERIALS AND METHODS

2.1. Materials and characterization

Ferrihydrite, goethite, and lepidocrocite were synthesized following the widely adapted methods by Cornell and Schwertmann (2004). Hematite synthesis followed the method by Lanzl et al. (2012). After synthesis, all mineral suspensions were centrifuged, washed with DI water until the electrical conductivity was less than 2 μS cm^{-1}, freeze-dried, and finely ground. The phase purity was confirmed by XRD (Fig. S1). Specific surface area was determined by Brunauer–Emmett–Teller (BET) gas adsorption method using a TriStar 3000 analyzer (Micromeritics Instrument Corporation, USA). Before the measurement, Fe oxide samples were degassed using He gas at 110 °C for 3 h. The BET surface areas of ferrihydrite, hematite, and goethite are 236 ± 1, 118 ± 1, and 38 ± 1 m^2 g^{-1}, respectively. The surface area of lepidocrocite was previously

reported to be 77 ± 1 m^2 g^{-1} using the same synthesis and measurement method (Davantès et al., 2016; Alexandratos et al., 2017).

Polyphosphate sodium salt (Na-polyP) was obtained from Sigma Aldrich. Its average chain length is estimated to be 10 by calculating the ratio of the peak area between the end P groups and middle P groups in its solution ^{31}P NMR spectrum (Fig. S2) following the reported method (Fang et al., 2015). We thus define the molecular formula of this polyphosphate sample as Na$_{12}$P$_{10}$O$_{31}$.

2.2. Polyphosphate hydrolysis

Three parallel sets of batch experiments were conducted to investigate polyphosphate reaction with Fe oxide minerals under varied solution chemistry: (1) DI water with 0.1 M NaCl at pH 6, 7.5, and 9 (Experimental Set 1); (2) DI water with 0.1 M NaCl and 1 mM Ca^{2+} at pH 6, 7.5, and 9 (Experimental Set 2); and (3) artificial seawater (ASW) at pH 8 (Experimental Set 3), as detailed below. All experiments were performed in duplicate.

For Experimental Set 1 (DI experiments), 0.04 g Fe oxides and 0.58 g NaCl (0.1 M) were mixed in 95 mL DI water in a glass bottle and equilibrated for 18 h under magnetic stirring. Experimental Set 2 (Ca^{2+} experiments) was conducted to explore the effects of Ca^{2+} on polyphosphate hydrolysis and transformation. 2 mL stock solution of CaCl$_2$ (50 mM) was first added into 93 mL DI water before the addition of 0.04 Fe oxides and 0.58 g NaCl. For these two experimental sets, the pH value of the suspension was constantly monitored and manually maintained at 6 ± 0.05, 7.5 ± 0.05, or 9 ± 0.05 using 0.05 M HCl or 0.05 M NaOH. For Experimental Set 3 (ASW experiments), ASW was prepared according to D1141-98 International Standard (ASTM D1141-98, 2013; Nguyen Dang et al., 2017) and contains 420 mM NaCl, 28.8 mM Na$_2$SO$_4$, 10.5 mM CaCl$_2$, 54.6 mM MgCl$_2$, 9.32 mM KCl, and 2.79 mM NaHCO$_3$. It has an initial pH of 8 ± 0.05. Prior to the experiment, 0.04 g Fe oxides were added in 95 mL ASW. The pH of the ASW-mineral suspension stayed stable at ~ 8 due to the strong buffering capacity of ASW. For all experimental sets, after overnight dispersion, 5 mL of polyphosphate stock solution (40 mM as total P) was added into the suspensions to achieve a final polyphosphate concentration of 2 mM as total P. This concentration was used to ensure the collection of ^{31}P solution NMR spectra with acceptable signal to noise ratio based on our recent studies (Huang et al., 2018; Wan et al., 2019b).

For all experiments, after the addition of polyphosphate stock solution to the Fe oxide suspension, pH of the suspension was immediately measured and adjusted to the desired value. After that, pH value of the reaction suspension was measured and adjusted several times (if needed) within the first 2 h and at 3, 5, 7, 10, 24, 48, 72, 96, 168, and 216 h (9 d) before 2 mL aliquot of the suspension was taken. The aliquot was immediately filtered through a 0.22-μm Millipore membrane. The supernatant was analyzed for orthophosphate and total P concentrations. For total P analysis, all P in the supernatant was hydrolyzed to inorganic orthophosphate via potassium persulfate

autoclave digestion (Das et al., 2014). Orthophosphate concentration was determined using the phosphomolybdate colorimetric assay (Murphy and Riley, 1962) on an UV–vis spectrometer (Carey 60; Agilent, USA). Concentration of Ca^{2+} in the supernatant was measured by inductively coupled plasma-optical emission spectrometry (ICP-OES; Optima 8000, PerkinElmer, USA). 10 μL of 5 mM sodium azide (NaN$_3$) solution was spiked to the suspension at a variety of time points. Sodium azide can effectively inhibit microbial growth and prevent potential influences from microbial activity (Cabrol et al., 2017; Skipper and Westermann, 1973).

To investigate the potential formation of apatite upon aging, long-term experiments were conducted on hematite and lepidocrocite with 1 or 2 mM polyphosphate (as total P) and Ca^{2+} at 1 or 2 mM at pH 9. Three aging experiments were conducted: *Sample 1* has 0.4 g L^{-1} hematite, 1 mM Ca^{2+}, 2 mM polyphosphate as total P, and 150-day reaction; *Sample 2* has 0.4 g L^{-1} hematite, 2 mM Ca^{2+}, 1 mM polyphosphate as total P, and 70-day reaction; *Sample 3* has 0.4 g L^{-1} lepidocrocite, 1 mM Ca^{2+}, 2 mM polyphosphate as total P, and 150-day reaction. Reaction procedure was the same as Experimental Set 2.

2.3. Solution and solid phase analyses

At the end of each reaction, the suspension was centrifuged to separate the solids and supernatant. The obtained wet pastes were washed twice with DI water and freeze-dried for analysis by XRD, FTIR, TEM, and P K-edge XAS, as detailed below.

XRD measurements were conducted on a Panalytical Empyrean diffractometer (Cu Kα radiation, $\lambda = 1.5418$ Å) using zero-background sample holders (MTI Corporation, USA). Scan parameters were 0.04° step size and 9 second/step at 5–80° 2θ. Synchrotron XRD data were collected at Beamline 11-ID-B (58.6491 keV, $\lambda = 0.2114$ Å) at the Advanced Photon Source (APS) at Argonne National Laboratory (Lemont, IL, USA), with a sample-to-detector distances of 100 cm.

FTIR analysis of the reaction products was conducted on a Thermo Scientific iS50 FT-IR Spectrometer via touch point one-touch sampling operation. Spectra were collected at 4000 to 500 cm^{-1} for an average of 64 scans at an instrument resolution of 4 cm^{-1}.

TEM and high angle annular dark-field (HAADF) images were collected on FEI Tecnai F30 TEM equipped with thermally assisted field emission gun and operated at 300 kV. A small quantity of powdered samples was dispersed in ethanol and ultrasonicated for 5 minutes. Around 10-μL aliquots of the suspension was placed on a carbon-coated copper grid and allowed to air dry. Elemental distribution maps were obtained for Ca and Fe from EELS spectral images using a power-law background model. Elemental abundance at selected points in HAADF image was record by an energy dispersion X-ray spectroscopy (EDS).

For NMR analysis, the supernatant obtained by centrifugation at the end of each experiment was further filtered by 0.22-μm Millipore membrane. Solution ^{31}P

NMR spectra were collected on a Bruker AMX 400 MHz spectrometer operated at 162 MHz and 297 K. Experimental parameters were 90° pulse width, 6.5 k data points (TD) over an acquisition time of 0.51 s, and 15 s relaxation delay. Chemical shift was calibrated using 85% H_3PO_4 as the external standard. At least 2048 scans (>2h) were collected for each spectrum.

Phosphorus K-edge XANES analysis was conducted at Beamline 14–3 at the Stanford Synchrotron Radiation Lightsource (SSRL), Menlo Park, CA, USA. Sample powders were brushed evenly onto P-free Kapton tape and mounted to a sample holder maintained under helium atmosphere. P XANES spectra were collected in fluorescence mode using a PIPS detector and at the energy range of 2100–2485 eV. Energy calibration used $AlPO_4$ (edge position at 2152.8 eV). A suite of P standard compounds were used for linear combination fitting (LCF) analysis. They are: (1) polyphosphate sodium salt (Na-polyP) and synthetic Ca-polyphosphate granules (Ca-polyP) (Wan et al., 2019b), representing solid polyphosphates. (2) orthophosphate-adsorbed on four Fe oxides, prepared at pH 6.0 using previously reported method (Wang et al., 2013a) and centrifuged after 6-h reaction, representing Fe oxide associated orthophosphate; (3) polyphosphate-adsorbed on four Fe oxides, prepared at pH 6.0 using the same method for preparing orthophosphate-adsorbed samples, representing Fe oxide associated polyphosphate; (4) amorphous calcium phosphate (ACP), octacalcium phosphate (octaCa), and hydroxyapatite (Huang and Tang, 2015), representing calcium phosphate minerals. P XANES spectra of all standard compounds were collected in the same manner as for unknown samples. XANES data analysis used the software Ifeffit (Ravel and Newville, 2005). All spectra were examined for energy calibration, merged, and normalized. LCF was conducted on the XANES spectra at energy range of –15 to 50 eV relative to the edge energy. The goodness of fit was evaluated using the residual factor (R-factor) and fits with the smallest R-factor were reported.

3. RESULTS

3.1. Polyphosphate adsorption and hydrolysis

Reaction of polyphosphate with Fe oxides leads to the degradation of polyphosphate and release of orthophosphate into the solution. Fig. 1 shows a typical kinetic curve of polyphosphate reaction on four Fe oxides in the absence/presence of 1 mM Ca^{2+}, similar to our previous observations on polyphosphate degradation on Al and Mn oxides (Wan et al., 2019a, b). Our previous study indicated that, without the addition of oxide minerals, only 2.8% of polyphosphate was degraded after 5-day control experiment in 0.5 mM Ca^{2+} solution (Wan et al., 2019a). Solution pH, presence of Ca^{2+}, and mineral type are found to influence the gradual release of orthophosphate from polyphosphate hydrolysis (Fig. 1). To directly compare the reaction on different Fe oxides, efforts were taken to quantitatively assess the reaction rate. We note that polyphosphate degradation is a complex process, involving initial adsorption onto the mineral surface, one-by-one cleavage of the

terminal phosphate groups (details in Section 3.2) and the subsequent production of orthophosphate and gradual shortening of polyphosphate chain, reaction of produced orthophosphate with the mineral surface (e.g., adsorption) and other dissolved cations (e.g., complexation with Ca^{2+}), as well as the reaction of unreacted or produced shorter-chained polyphosphates with the mineral surface and other dissolved cations. The observed orthophosphate concentration in the supernatant is a net result of these reactions.

As observed in our previous studies (Wan et al., 2019a, b) and detailed later, polyphosphates outcompete and replace orthophosphate in adsorption on the mineral surfaces as polyphosphate molecules contain more phosphate groups and higher negative charge. Thus the observed concentration of orthophosphate in the solution is dominated by the contribution from polyphosphate hydrolysis in the absence of complexing cations. To enable quantitative comparison across experiments, we assigned the observed rate of orthophosphate concentration change/production (Fig. 1) as the apparent hydrolysis rate. We then conducted kinetic fitting on the observed apparent hydrolysis rate and best fitting results were obtained using first-order kinetic model (Fig. S3 and Table 1). The R^2 values are 0.905–0.998 for pH 6 and 7.5 and 0.842–0.991 for pH 9 (Table 1). The relatively lower R^2 values for pH 7.5 and 9 experiments in the presence of Ca^{2+} is likely due to the formation of Ca-phosphate ternary surface complexes/precipitates (Li et al., 2012; Wan et al., 2016; Wan et al., 2017b), which decreases orthophosphate concentration in the supernatant and thus the goodness of fit.

In the absence of Ca^{2+} (Fig. 2), the apparent hydrolysis rates are ~ 0.25×10^{-3} h^{-1} for ferrihydrite, hematite, and goethite. Lepidocrocite shows a high rate, which increases from 0.35×10^{-3} h^{-1} at pH 6 to 1.14×10^{-3} h^{-1} at pH 9. This is similar to previously observed higher reactivity of lepidocrocite than other Fe or metal oxide minerals for the degradation of tris(1,3-dichloro-2-propyl) phosphate, a typical phosphate triester (Fang et al., 2018). Then, the apparent hydrolysis rates are normalized by specific surface area of Fe oxides and the surface area-normalized hydrolysis rates are between 4.28 and 74.03×10^{-6} mM h^{-1} m^{-2} (Table 1). For surface area normalized apparent hydrolysis rate, lepidocrocite shows the highest rate and the order of rate for different Fe oxides is roughly lepidocrocite > goethite > hematite > ferrihydrite.

The presence of Ca^{2+} significantly increases orthophosphate production for all four Fe oxides and the highest level of orthophosphate release is observed at pH 7.5 with 9-d reaction (Fig. 1). In the presence of 1 mM Ca^{2+}, the hydrolysis extent roughly follows the order of lepidocrocite > hematite > ferrihydrite > goethite (Fig. 1). For example, with Ca^{2+} at pH 7.5, orthophosphate release reaches 884 μM (46.4% of total P loading), 670 μM (40.4%), 489 μM (38.5%), and 324 μM (15.8%) for lepidocrocite, hematite, ferrihydrite, and goethite, respectively (Figs. 1 and S4). Meanwhile, the apparent hydrolysis rate also increases for all four Fe oxides in the presence of Ca^{2+} (Fig. 2 and Table 1), which is affected by solution pH. At pH 6 and 7.5, the enhancement of polyphosphate apparent
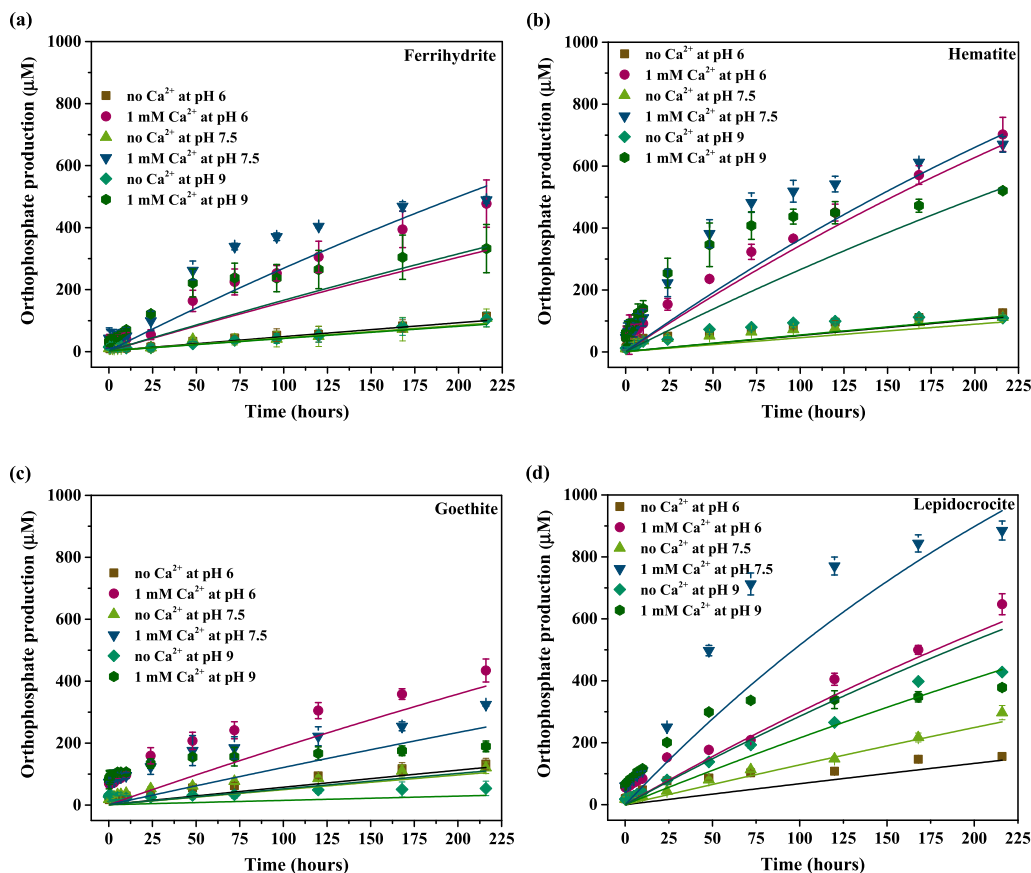
Fig. 1. Dynamics of orthophosphate production in solution during polyphosphate interaction with ferrihydrite (a), hematite (b), goethite (c), and lepidocrocite (d) in the absence/presence of 1 mM Ca^{2+} at pH 6, 7.5, and 9. The error bars represent the standard deviation (n = 2). Lines present the fitting results of first order kinetic model for orthophosphate production.

Table 1
First-order kinetic fitting results of the apparent hydrolysis rates of polyphosphate on Fe oxides under various solution conditions (Fig. S3).

| PolyP | Experimental condition | | | Reaction time (h) | k ($10^{-3}h^{-1}$) | Area-normalized rate (10^{-6} mM h^{-1} m^{-2}) | R^2 |
	Mineral	pH	Ca^{2+}				
P_{10}	Ferrihydrite	6	–	216	0.232	4.96	0.985
P_{10}	Ferrihydrite	6	1 mM	216	0.818	17.33	0.992
P_{10}	Hematite	6	–	216	0.264	11.28	0.938
P_{10}	Hematite	6	1 mM	216	1.88	80.34	0.998
P_{10}	Goethite	6	–	216	0.287	37.76	0.989
P_{10}	Goethite	6	1 mM	216	0.984	129.47	0.977
P_{10}	Lepidocrocite	6	–	216	0.345	22.4	0.906
P_{10}	Lepidocrocite	6	1 mM	216	1.62	105.19	0.990
P_{10}	Ferrihydrite	7.5	–	216	0.210	4.45	0.959
P_{10}	Ferrihydrite	7.5	1 mM	216	1.43	30.3	0.924
P_{10}	Hematite	7.5	–	216	0.226	9.66	0.948
P_{10}	Hematite	7.5	1 mM	216	2.0	85.47	0.915
P_{10}	Goethite	7.5	–	216	0.246	32.37	0.943
P_{10}	Goethite	7.5	1 mM	216	0.620	81.58	0.970
P_{10}	Lepidocrocite	7.5	–	216	0.665	43.18	0.992
P_{10}	Lepidocrocite	7.5	1 mM	216	2.98	193.51	0.905
P_{10}	Ferrihydrite	9	–	216	0.202	4.28	0.966
P_{10}	Ferrihydrite	9	1 mM	216	0.851	18.03	0.892
P_{10}	Hematite	9	–	216	0.271	11.58	0.875
P_{10}	Hematite	9	1 mM	216	1.42	60.68	0.853
P_{10}	Goethite	9	–	216	0.07	9.21	0.858
P_{10}	Goethite	9	1 mM	216	0.259	34.08	0.842
P_{10}	Lepidocrocite	9	–	216	1.14	74.03	0.991
P_{10}	Lepidocrocite	9	1 mM	216	1.54	100	0.873
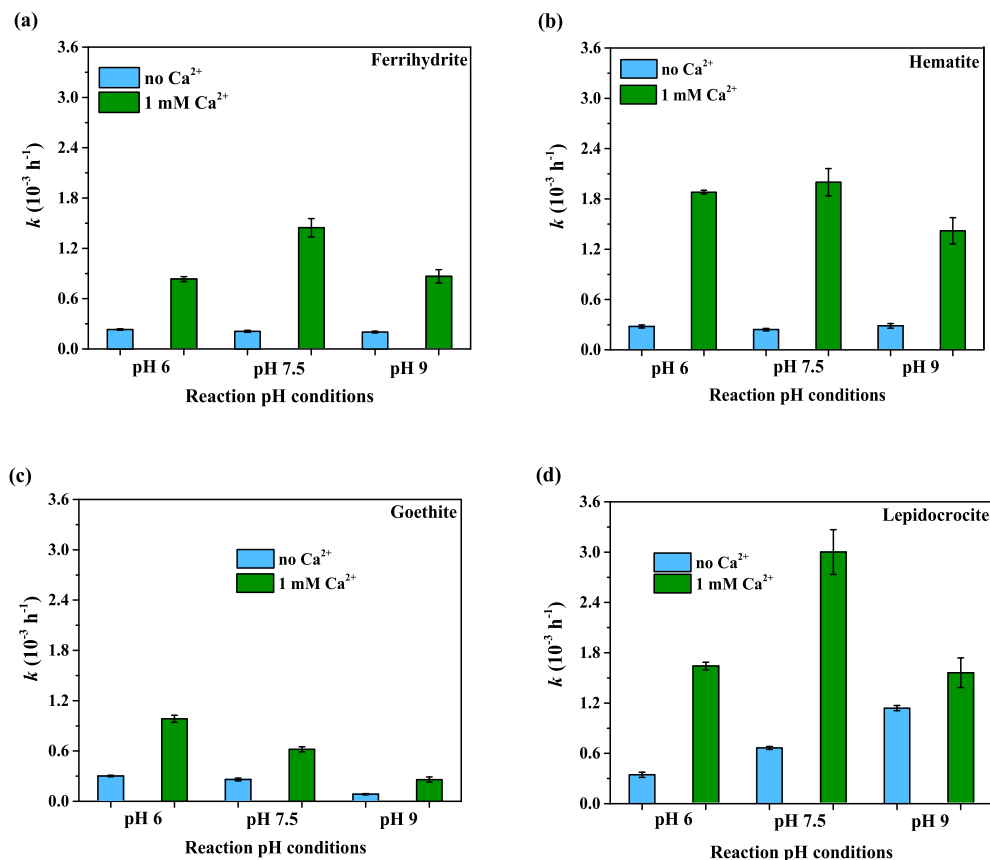
Fig. 2. Apparent hydrolysis rates of polyphosphate on Fe oxides (a: ferrihydrite; b: hematite; c: goethite; and d: lepidocrocite) in the absence/presence of 1 mM Ca^{2+} at pH 6, 7.5, and 9. The dynamics of orthophosphate production were fitted by first-order kinetic model to obtain apparent hydrolysis rates. Error bars represent standard deviation (n = 2).

hydrolysis rate increases relative to those at pH 9. The low hydrolysis rate at pH 9 may be attributed to the potential formation of calcium phosphate minerals and/or surface ternary complexes that reduces the release of orthophosphate into the supernatants. In the presence of Ca^{2+}, surface area-normalized apparent hydrolysis rates for four Fe oxides are between 17.33 and 193.51 $\times$ 10^{-6} mM h^{-1} m^{-2}. The rate roughly follows the order of lepidocrocite $\approx$ goethite $>$ hematite $>$ ferrihydrite at pH 6 and lepidocrocite $>$ goethite $\approx$ hematite $>$ ferrihydrite at pH 7.5 and 9 (Table 1).

We also monitored the dynamics of total P concentration in the supernatants (Fig. S4). At pH 6 and 7.5, polyphosphate rapidly absorbs on ferrihydrite, hematite, goethite, and lepidocrocite during the first 10 h. As the reaction proceeds, subsequent polyphosphate hydrolysis and orthophosphate release lead to the increase of total P concentration in the supernatant (Fig. S4), consistent with our previous studies (Wan et al., 2019a, b). Interestingly, in ferrihydrite suspension, total P concentration continuously decreases at all three pH values within the 9-day reaction, likely due to a large amount of orthophosphate and polyphosphate adsorption on ferrihydrite, which has high surface area and reactivity toward P adsorption (Wang et al., 2013a; Wang et al., 2017). At pH 6 and 7.5, the presence of Ca^{2+} decreases the total P concentration in the supernatant, likely due to the formation of surface ternary complex(es) (Li et al., 2012; Wan et al., 2019b), which subsequently facilitates polyphosphate/orthophosphate uptake by Fe oxide surfaces (Fig. S4). At pH 9, a different trend of total P concentration is observed: the presence of 1 mM Ca^{2+} significantly reduces total P concentration at 10 h to 9 d (Fig. S4). Within 9-day reaction, Ca^{2+} concentration gradually decreases, reaching $\sim$ 400 μM at pH 9 (Fig. S5). At this pH, the simultaneous decrease of Ca^{2+} and total P concentrations suggests the potential formation of calcium phosphate precipitates, as discussed in Section 3.2.

3.2. Polyphosphate transformation on Fe oxide surface

To reveal the hydrolysis mechanism, we conducted solution ^{31}P NMR to characterize aqueous P speciation in the 9-d reaction supernatants (Fig. 3) and P K-edge XANES to determine the complexation state and phase of P species in the solid products (Figs. 4 and 5). In the absence of Ca^{2+}, the chemical shifts associated with polyphosphate terminal P groups (at around $-$ 8 ppm) and middle P groups (at around $-$ 21.7 ppm) are observed (Fig. 3a-c). The chemical shift at $\sim$ 1 ppm is attributed to orthophosphate in the supernatants. As pH increases from 6 to 9, the chemical shifts of these two P environments gradually shift to lower field since the protonation level of orthophosphate and
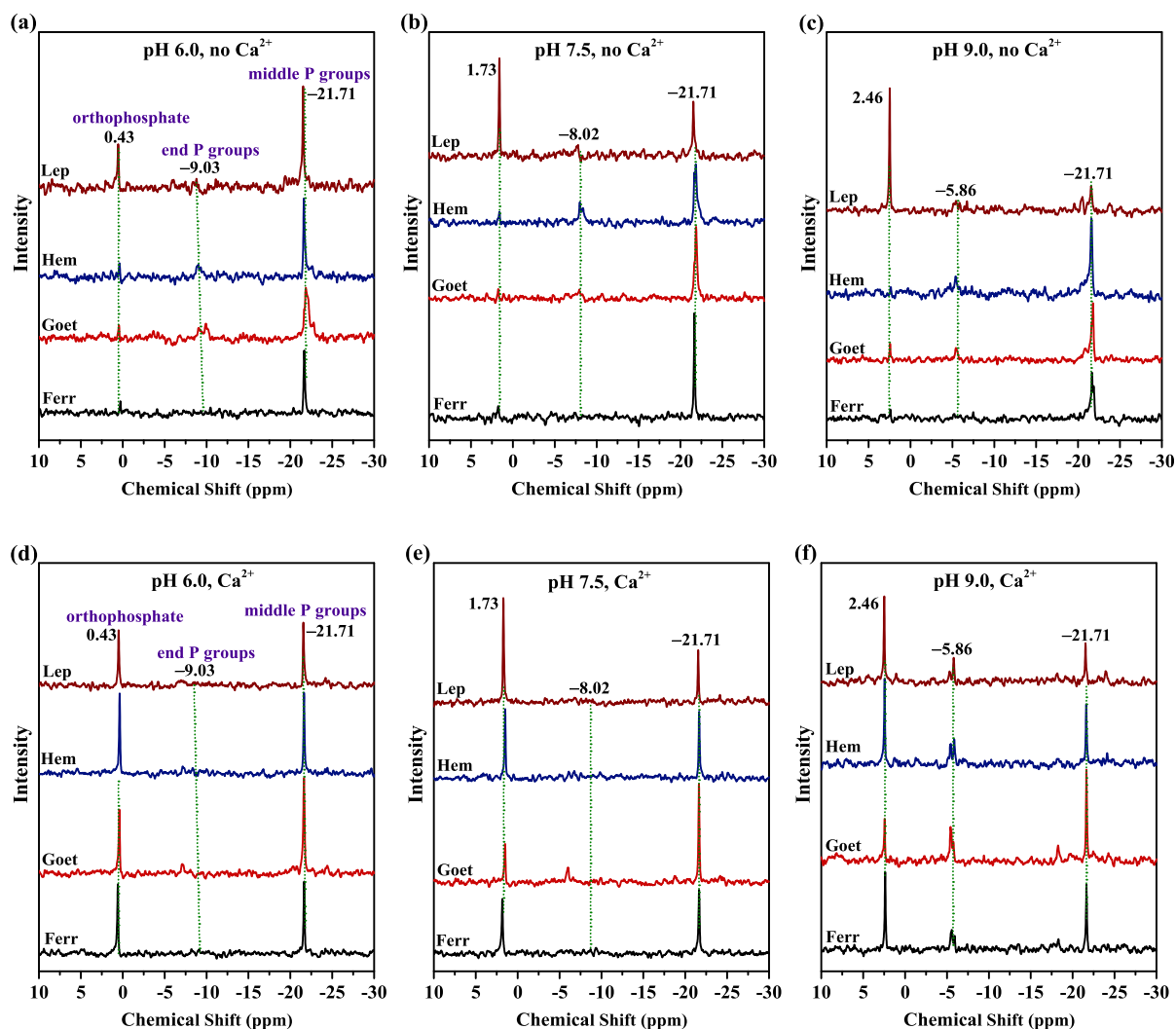
Fig. 3. ^{31}P solution NMR spectra of the liquid supernatants after 9-day interaction of polyphosphate with Fe oxides at pH 6 (a, d), 7.5 (b, e), and 9 (c, e) in the absence (a-c) or presence (d-f) of 1 mM Ca^{2+}. Abbreviations: Ferr: ferrihydrite; Hem: hematite; Goet: goethite; and Lep: lepidocrocite.

polyphosphate terminal P groups correspondingly decreases. A previous study demonstrated that, as solution pH increased from 5 to 13, NMR chemical shifts increased from 0.7 to 7 for orthophosphate, −9.9 to − 3.8 for terminal P groups of polyphosphate, and − 21.7 to − 20.6 for middle P groups of polyphosphate, respectively (McDowell and Stewart, 2005). In our study, the chemical shifts increased from 0.43 to 2.46 ppm for orthophosphate and from − 9.03 to − 5.86 ppm for the terminal phosphate groups of polyphosphate (Fig. 3a-c). However, in the supernatant of the lepidocrocite suspension, the intensity of chemical shift for orthophosphate increases significantly as pH increases from 6 to 9, suggesting the gradual increase of orthophosphate production due to polyphosphate hydrolysis. The chemical shift of orthophosphate at 2.46 ppm dominates solution ^{31}P NMR spectrum for reaction on lepidocrocite at pH 9 (Fig. 3c), suggesting the high reactivity of lepidocrocite toward polyphosphate hydrolysis, which increases with increasing pH, and is consistent with the observed trend in batch experiments (Fig. 2d).

In the presence of Ca^{2+}, solution ^{31}P NMR shows results consistent with batch experiments, in that Ca^{2+} significantly promotes polyphosphate hydrolysis (Fig. 3d-f). For example, in the presence of 1 mM Ca^{2+}, the chemical shift of orthophosphate becomes dominant in the NMR spectra of supernatants for all Fe oxides. For hematite and lepidocrocite at pH 7.5 and 9, the intensity of orthophosphate chemical shift at ~ 1 ppm is much stronger than that of polyphosphate middle P groups. This indicates that the concentration of orthophosphate is higher than polyphosphate in the supernatants and most of polyphosphate is hydrolyzed after 9-d reaction in the presence of Ca^{2+}. Solution ^{31}P NMR spectra of all supernatants in Fig. 3 did not show the random appearance of shorter chained polyphosphates, which would have led to the occurrence of multiple chemical shifts at around − 21 ppm (middle groups of polyphosphates with varied chain lengths), as we have previously discussed in details (Huang et al., 2018; Wan et al., 2019a, b). Combined with the continuous production of orthophosphate in the
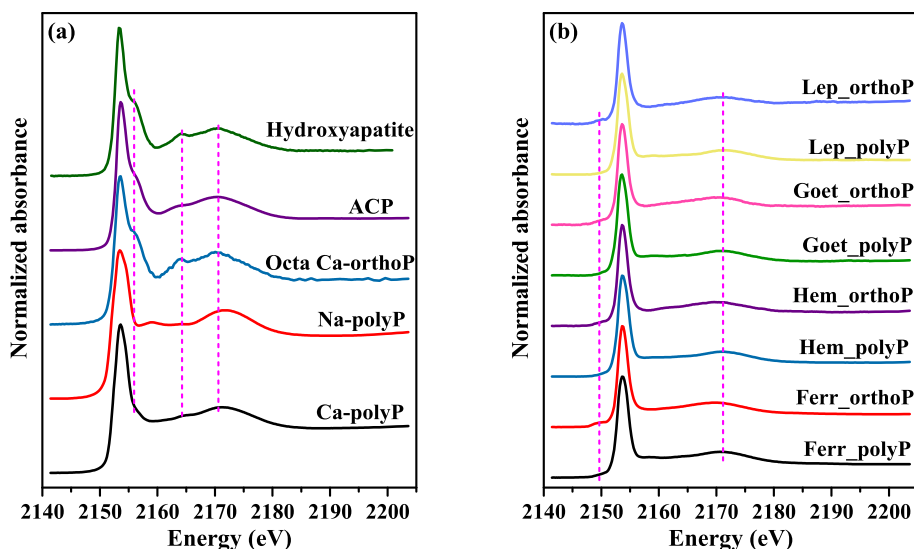
Fig. 4. Normalized P K-edge XANES spectra of different P standard compounds for LCF analysis: a) P-containing salts or precipitates; b) P adsorbed on Fe oxides. Abbreviations: ACP: amorphous calcium phosphate; Octa Ca-orthoP: octacalcium phosphate; Na-polyP: sodium polyphosphate; Ca-polyP: calcium polyphosphate; Ferr_polyP: ferrihydrite-adsorbed polyphosphate; Ferr_orthoP: ferrihydrite-adsorbed orthophosphate; Hem_polyP: hematite-adsorbed polyphosphate; Hem_orthoP: hematite-adsorbed orthophosphate; Goet_polyP: goethite-adsorbed polyphosphate; Goet_orthoP: goethite-adsorbed orthophosphate; Lep_polyP: lepidocrocite-adsorbed polyphosphate; Lep_orthoP: lepidocrocite-adsorbed orthophosphate.

reaction suspensions (Fig. 1), ^{31}P NMR results suggest that a terminal-only hydrolysis pathway is the dominant mechanism for polyphosphate hydrolysis on Fe oxides, where orthophosphate is produced via one-by-one cleavage of terminal $P - O - P$ bonds in polyphosphate molecules, similar to the cases of enzyme-, Al oxide-, and Mn oxide-catalyzed polyphosphate hydrolysis (Huang et al., 2018; Wan et al., 2019a, b).

Since P K-edge XANES spectra of phosphates adsorbed on Fe oxides have different features compared to calcium phosphate minerals (Fig. 4), we conducted P XANES to identify and quantify surface P species in the solid products. P XANES spectra of calcium phosphate mineral or polyphosphate compounds have post-edge characteristics that are different from varied P standard compounds (Fig. 4a). The spectra of orthophosphate or polyphosphate adsorbed on Fe oxides show a minor pre-edge feature at $- 5$ to $- 1$ eV (relative to edge position) and lack the post-edge characteristics (Fig. 4b), due to the electronic transition of a P 1 s electron into an Fe(3d)-O(2p)-P(3p) antibonding molecular orbital (Khare et al., 2005). Therefore, P K-edge XANES can be useful in identifying solid P species especially for systems containing both Fe and Ca phosphate phases (Huang and Tang, 2016).

In the absence of Ca^{2+}, P XANES spectra of polyphosphate reacted with Fe oxides are similar to their corresponding polyphosphate or orthophosphate-adsorbed standard compounds (Figs. 4 and S6), suggesting that the main P species in these products are adsorbed phosphates via inner-sphere complexation on Fe oxide surface (Abdala et al., 2015a; Abdala et al., 2015b). However, in the presence of Ca^{2+}, the main peak at 2155.8 eV broadens (Fig. 5e) and a small shoulder peak at ∼ 2164 eV appears in

the spectra of solid reaction products at pH 9 (Fig. 5a-d, with zoomed view of the post-edge region in Fig. 5e). These characteristics suggest the presence of newly formed calcium phosphate minerals. Additionally, P XANES spectra do not show well-separated shoulder peaks at ~2164 eV, suggesting that the formed calcium phosphate minerals are amorphous phase and not crystalline (Huang et al., 2018; Wan et al., 2019b). We then conducted LCF analysis of the sample XANES spectra using representative standard compounds, including ACP solids, Ca-polyphosphate, Na-polyphosphate, and polyphosphate/ orthophosphate adsorbed on Fe oxides. LCF results show that, as pH increases from 6 to 9, ACP contents increase from 22.6% to 56% for ferrihydrite, from 8.3% to 26.6% for hematite, from 0 to 17.1% for goethite, and from 3.9% to 45.5% for lepidocrocite (Fig. S6). At pH 9, P XANES spectra of the solid products show the highest ACP contents (Fig. 5a-d). Thus, ^{31}P NMR and P XANES analyses suggest that the short term transformation pathway of polyphosphate on Fe oxides includes polyphosphate adsorption as inner-sphere surface complexes, polyphosphate hydrolysis and orthophosphate release, and the precipitation of orthophosphate with Ca^{2+} to form ACP phase, which is consistent with our previous studies (Wan et al., 2019a, b).

3.3. Formation of crystalline calcium phosphate minerals upon aging

Although the formation of ACP is observed during the 9-day reaction period in the presence of Ca^{2+}, whether ACP can transform into crystalline phosphate minerals (e.g., hydroxyapatite) in this system remains unclear. We
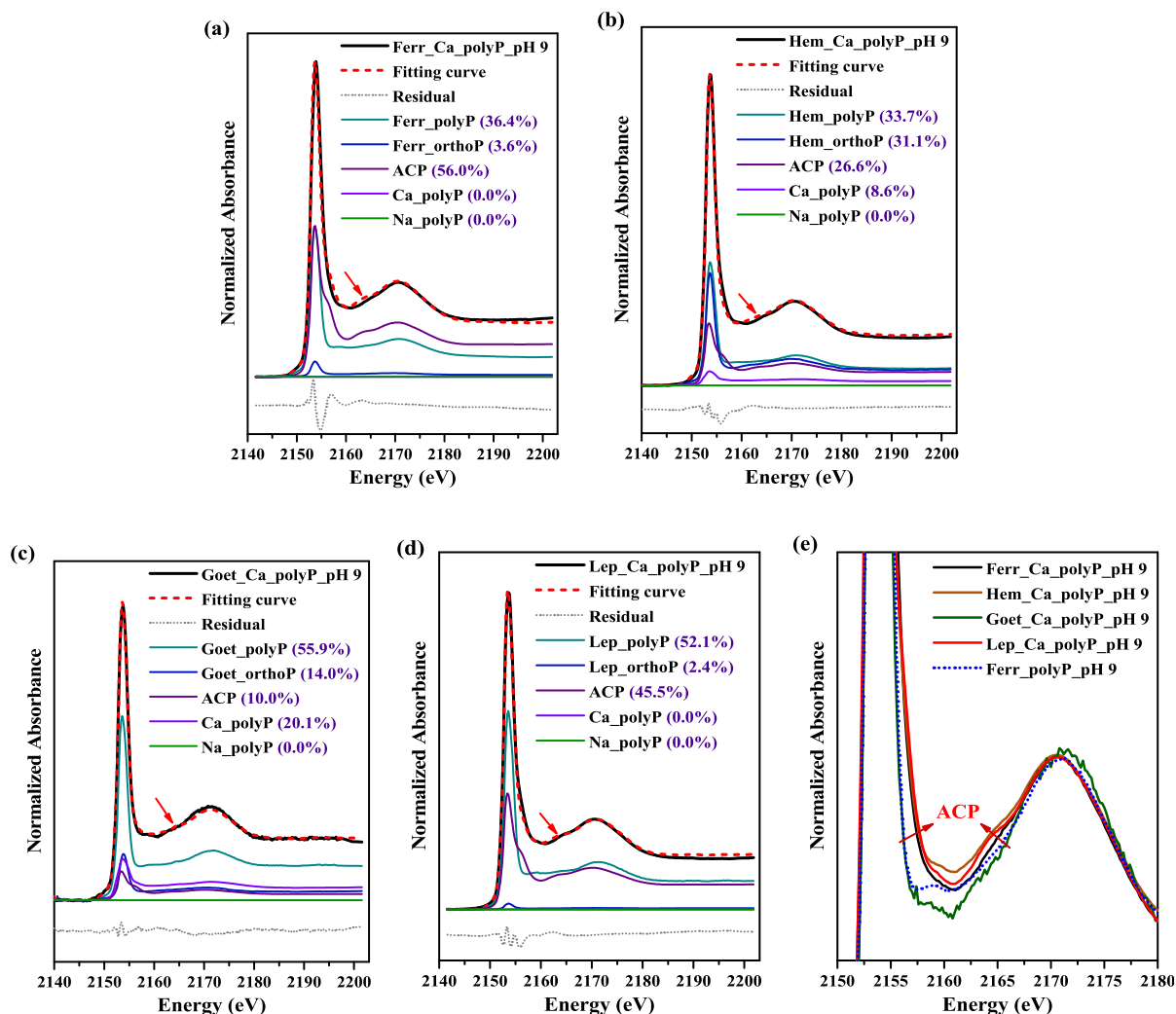
Fig. 5. Results of LCF analysis of P XANES spectra of the 9-day products from polyphosphate reaction with ferrihydrite (a), hematite (b), goethite (c), and lepidocrocite (d) in the presence of 1 mM Ca^{2+} at pH 9. Raw and fitted data are in black solid and red dotted lines, respectively. Panel (e) is a zoomed view of the post-edge features in comparison with the P XANES spectrum of polyphosphate adsorption on ferrihydrite (9-day reaction time). Red arrow indicates the post-edge features of amorphous calcium phosphate (ACP).

hypothesize that long-time aging of the produced ACP solids might lead to the formation of crystalline calcium phosphate phases, which can help explain the wide occurrence of crystalline apatite in aquatic environment. Indeed, for the three aged samples with 70- or 150-day reaction time (*Samples 1–3*; details in Experimental section and Table 2), their P XANES spectra show the formation of hydroxyapatite upon long-term aging (Fig. 6a). For the hematite sample (*Sample 2*) aged for 70 days with 2 mM Ca^{2+} and 1 mM polyphosphate (as total P), we observed the obvious separation in peaks at ~ 2164 eV that can be attributed to crystalline calcium phosphate minerals (Fig. 6a). P XANES spectra of calcium phosphate standard compounds usually have two distinct post-edge shoulders (+2 eV and + 11 eV relative to edge position) which become less distinctive with decreasing crystallinity (Fig. 4a) (Brandes et al., 2007; Franke and Hormes, 1995). LCF results show that the percentage of hydroxyapatite is 11.2% for *Sample 1*, 83.9% for

Sample 2, and 30.3% for *Sample 3* (Table 2). Meanwhile, these samples also contain surface adsorbed phosphate and ACP. After aging at 70 days or longer time, the hydrolysis of polyphosphate is expected to be close to completion (as supported by FTIR data discussed below), although LCF shows some minor amounts of adsorbed polyphosphate.

Laboratory XRD patterns of the three aged samples do not show diffraction peaks of crystalline phosphate minerals (Fig. S7a), likely due to the low crystallinity and relatively small amount of newly formed hydroxyapatite as compared to the background signal from highly crystalline hematite and lepidocrocite. Thus we further conducted synchrotron XRD analysis of these three samples. *Sample 2* (hematite, 1 mM polyphosphate as total P, 2 mM Ca^{2+}, 70-day aged) shows weak diffraction peaks belonging to hydroxyapatite (002) and (211) planes at 0.34 and 0.28 nm d-spacing (Fig. 6b). These peaks are not observed

Table 2

Results of linear combination fitting (LCF) analysis of P K-edge XANES spectra of the solid products after long term reaction of polyphosphate with hematite or lepidocrocite in the presence of Ca^{2+} at pH 9 (Fig. 6a).

Sample label	Reaction condition	Relative percentage (%)						R-factor
		HAP	ACP	Adsorbed orthoP	Adsorbed polyP	Ca_polyP	Na_polyP	
Sample 1	Hematite, 1 mM Ca^{2+}, 2 mM polyP (as total P), 150 days	11.2 ± 1.8	37 ± 7.6	26.3 ± 1	18.0 ± 0.8	N/A	0.075 ± 5.9	0.0005
Sample 2	Hematite, 2 mM Ca^{2+}, 1 mM polyP (as total P), 70 days	83.9 ± 21.7	N/A	11.1 ± 5	5.0 ± 6.2	N/A	N/A	0.0063
Sample 3	Lepidocrocite, 1 mM Ca^{2+}, 2 mM polyP as total P, 150 days	30.3 ± 2	20.8 ± 10.8	46.6 ± 4.7	N/A	N/A	2.2 ± 7.3	0.0007

for the other two samples containing high percentages of ACP and low percentages of hydroxyapatite determined by LCF of P XANES data (Table 2).

FTIR spectroscopy was applied to further reveal surface P speciation and to distinguish adsorbed P species and solid P minerals in the IR region of 1450–600 cm^{-1}, which originates primarily from the stretching vibrations of surface phosphate groups (Fig. 6c) (Wan et al., 2016). Compared with the corresponding IR spectra of unreacted Fe oxides, the abundant P absorbance bands below 1200 cm^{-1} belong to orthophosphate asymmetrical and symmetrical vibrations (Elzinga and Sparks, 2007; Wan et al., 2016). We did not observe the feature IR bands of P $-$ O $-$ P vibration in polyphosphate molecules beyond 1220 cm^{-1} (Michelmore et al., 2000; Wan et al., 2017a), suggesting the complete hydrolysis of polyphosphate after long-time aging of 70 or 150 days. For *Sample 2* (hematite, Ca:P ratio of 1:2, 70-day aging), four IR absorbance bands at 1112, 1026, 961, and 871 cm^{-1} appear, and the band positions and spectrum shape are similar to those of hydroxyapatite (Wan et al., 2016). For other two samples, in addition to IR bands of hydroxyapatite or ACP, we observed two main IR peaks at 1101 and 913 cm^{-1}, which can be assigned to the vibrations of inner-sphere orthophosphate complexes on Fe oxide surface (Elzinga and Sparks, 2007). FTIR results indicate the presence of hydroxyapatite and orthophosphate surface complexes on Fe oxides as the two main surface P species and the complete hydrolysis of polyphosphate on Fe oxides upon long-term aging. ACP has a single IR peak at ~ 1026 cm^{-1} that overlaps with the IR bands of hydroxyapatite (Skrtic et al., 2002) and thus cannot be distinguished here (Fig. 6c). A shorter aging time and a higher Ca:P ratio (2:1) of *Sample 2* as compared to the other two samples suggest that aging is a necessary step for ACP transformation to crystalline hydroxyapatite and that excess phosphate ions might inhibit the transformation.

TEM was applied to visualize the presence and distribution of hydroxyapatite in *Sample 2* that is dominated by hydroxyapatite and hematite. TEM images show large aggregated particles in the reaction products (Fig. 6d). In selected region (Fig. 6e), high resolution TEM shows the presence of two different mineral phases with lattice fringes at 0.37 nm d-spacing that belongs to the (012) plane of hematite, as well as 0.34 nm and 0.28 nm that belong to the (002) and (211) planes of hydroxyapatite. Selected area electron diffraction (SAED) shows the diffraction rings for hematite (012) and (110) as well as hydroxyapatite (002) and (211) (Fig. 6f). The distribution of hydroxyapatite and hematite was characterized by EELS elemental maps of Ca (Fig. 6g) and Fe (Fig. 6h). Iron and Ca maps can be used to infer the distribution of hematite and hydroxyapatite, since these are the main mineral phases determined by synchrotron XRD, FTIR, and P XANES. The Ca map shows non-uniform distribution and abundance (reflected by color intensity) of hydroxyapatite (Fig. 6g). The Fe map shows more uniform distribution of hematite (Fig. 6h). RBG color maps of Ca and Fe show the presence of hydroxyapatite on hematite surface (Fig. 6i). Due to the strong aggregation of hematite particles, the image region
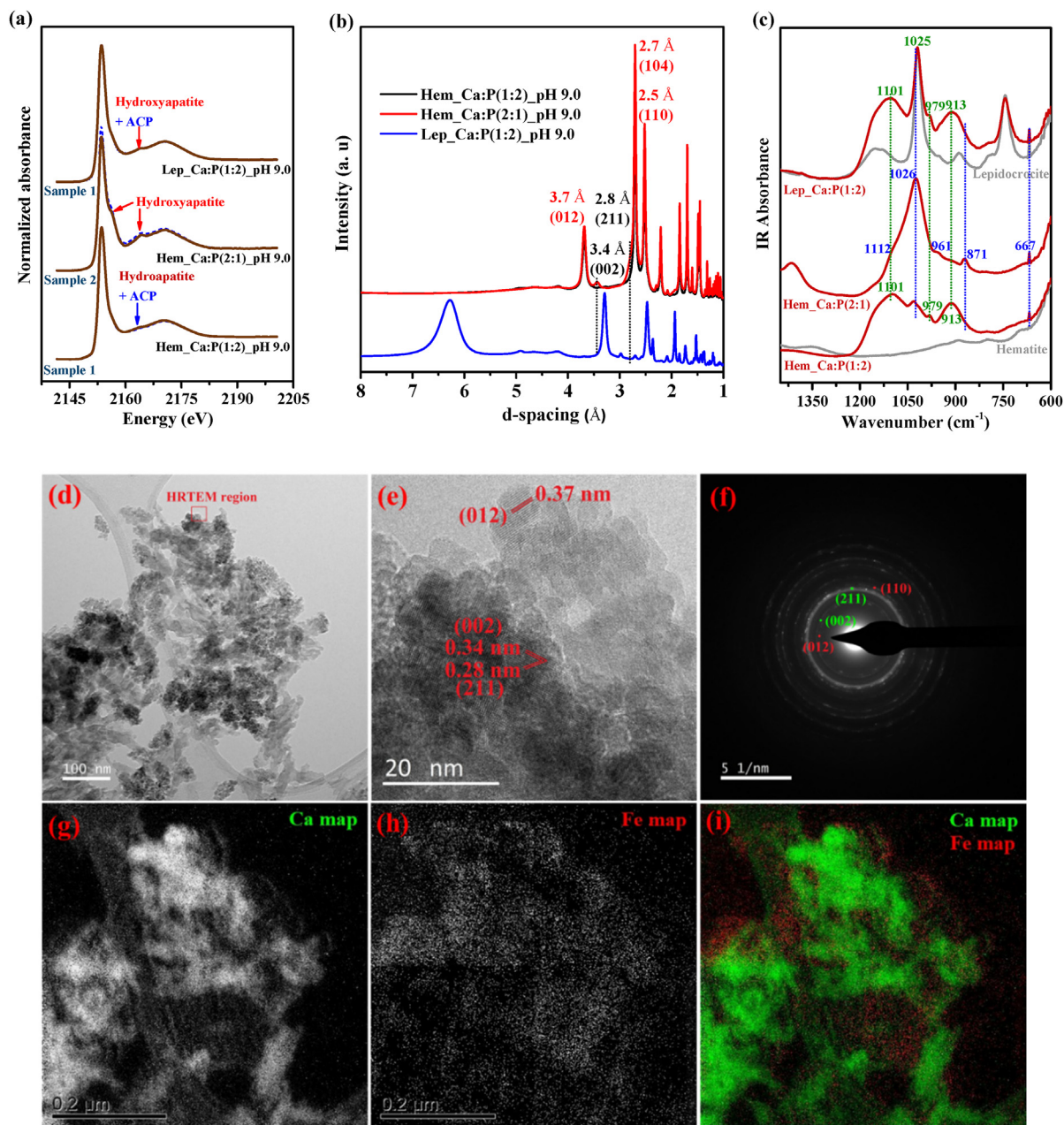
Fig. 6. Phosphorus (P) K-edge XANES (a), synchrotron XRD (b), and FTIR (c) data of the aged reaction products upon polyphosphate interaction with hematite and lepidocrocite in the presence of Ca^{2+} (1 or 2 mM) at pH 9. For P XANES LCF analysis, raw and fitted data are in grey solid and blue dotted lines, respectively. Panel (d) is TEM image of sample Hem_Ca:P(2:1)_pH 9.0, with HRTEM image of the selected region (e) and its electron diffraction pattern (f). Panel (i) is RBG EELS maps of Ca (g) and Fe (h), indicating the co-existence of hematite and hydroxyapatite, which is further validated by synchrotron XRD analysis. Notes: Ca:P(1:2) indicates 1 mM Ca^{2+} and 2 mM polyphosphate as total P; Ca:P(2:1) indicates 2 mM Ca^{2+} and 1 mM polyphosphate as total P.

in Fig. 6d might contain relatively few hematite particles, leading to a low intensity of Fe signal (Fig. 6h). To prove this, we selected another region to collect EELS elemental maps of Ca and Fe (Fig. S7b-f) and collected high-angle annular dark field-scanning transmission electron microscopy (HAADF-STEM) image in the larger region and EDS spectra for three selected points (Fig. S8). In the EELS maps, we found aggregated particles containing high contents of hematite with minor amounts of hydroxyapatite distributed on hematite surface (Fig. S7d-f). In HAADF-STEM image with EDS spectra, Points 1 and 2 indicate some large aggregated hematite particles with surface associated Ca^{2+} and orthophosphate (Fig. S8). The dark particle indicated by Point 3 has a high concentration of Ca and

P, implying the co-existence of fine hydroxyapatite particles that randomly distributed in the products (Fig. S8).

3.4. Reactions in artificial seawater

As mentioned earlier, polyphosphate transformation plays a key role in geologic P sequestration and marine P burial (Diaz et al., 2008; Huang et al., 2018; Omelon and Grynpas, 2008). Natural waterbodies (fresh water and seawater) typically have high concentrations of Ca^{2+} (~0.8 mM for fresh water and ~ 10.5 mM for seawater) (Nguyen Dang et al., 2017; Yuan et al., 2019), which might enhance polyphosphate hydrolysis and transformation on environmental minerals. Therefore we conducted polyphosphate hydrolysis experiments on Fe oxides in ASW in order to investigate polyphosphate transformation under marine conditions (Fig. 7). The results show that polyphosphate is gradually hydrolyzed on four Fe oxides in ASW (Fig. 7a) and the apparent hydrolysis rate can be fitted using first-order kinetic model (Fig. S9a and Table 3). The extent and rate of the apparent hydrolysis follow the order of lepidocrocite > hematite > ferrihydrite ≥ goethite (Fig. 7a and S9a). Surface area normalized apparent hydrolysis rates are between 6.08 and 58.51 × 10^{-6} mM h^{-1} m^{-2} and in the order of lepidocrocite > goethite > hematite > ferrihydrite (Table 3). Although the mineral reactivity order for polyphosphate hydrolysis in ASW is in line with that in the presence of 1 mM Ca^{2+} in DI water, the absolute values of rate and extent (at pH 8 for ASW) are smaller than those at pH 7.5 or 9 in DI (Fig. 1, Tables 1 and 3). In ASW, the significant decrease of apparent hydrolysis rate can be attributed to the high salinity of ASW. Polyphosphate hydrolysis by
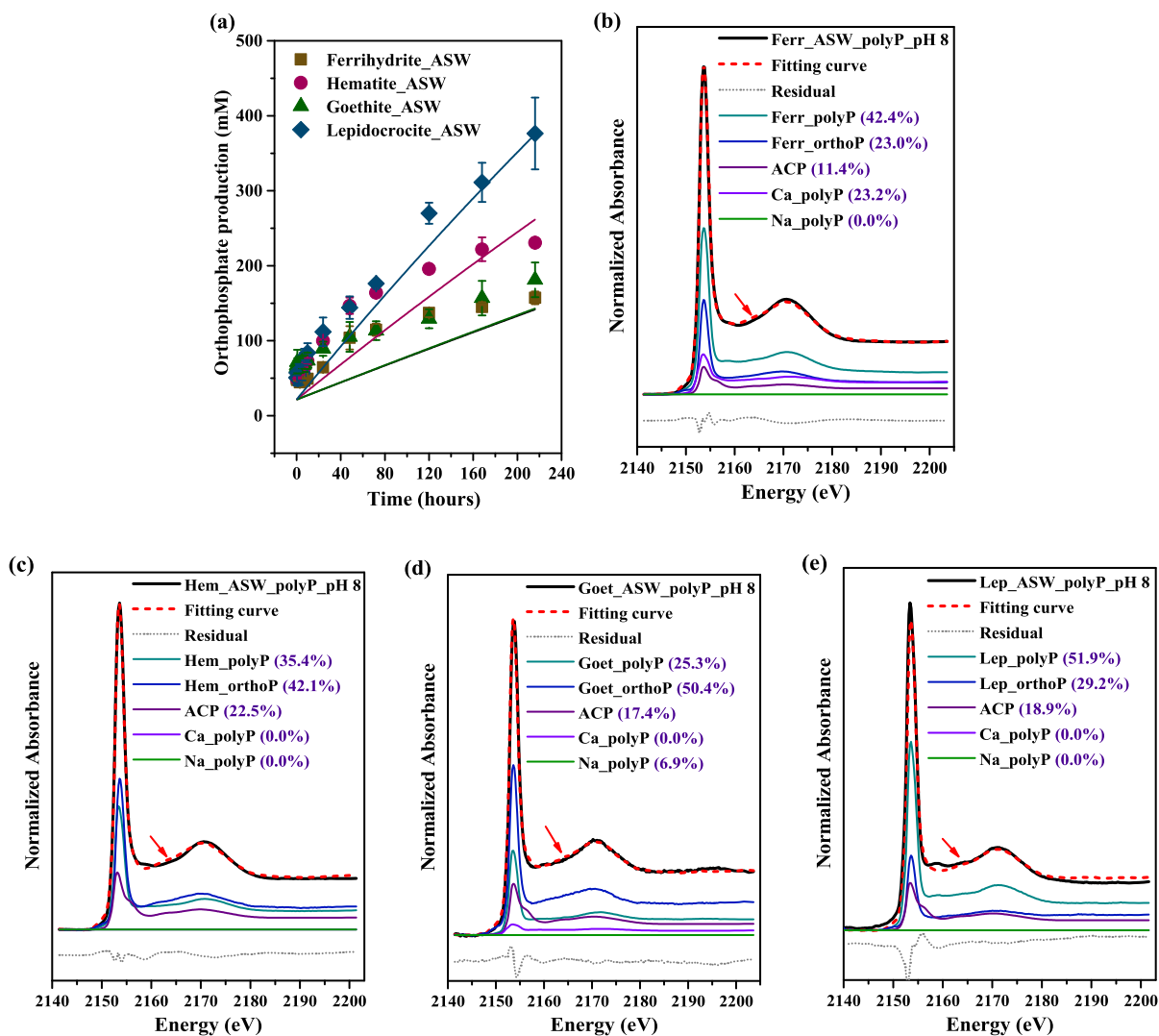

Fig. 7. (a) Dynamics and first-order kinetic fitting results of polyphosphate hydrolysis on ferrihydrite, hematite, goethite, and lepidocrocite in artificial seawater. Error bars represent standard deviation (n = 2). Lines present the fitting results using first order kinetic model for orthophosphate production. Panels (b–e) are LCF of P XANES spectra of polyphosphate 9-day reaction products on ferrihydrite, hematite, goethite, and lepidocrocite in ASW, respectively. Raw and fitted data are in black solid and red dotted lines, respectively. Red arrow indicates the post-edge features of amorphous calcium phosphate (ACP).

Table 3
First-order kinetic fitting parameters of the apparent hydrolysis rates of polyphosphate on Fe oxides in artificial seawater (Fig. S9a).

Experimental condition				Reaction time (h)	k (10^{-3}h^{-1})	Area-normalized rate (10^{-6} mM h^{-1} m^{-2})	R^2
PolyP	Mineral	pH	Ca^{2+}				
P$_{10}$	Ferrihydrite	8	10.5 mM	216	0.287	6.08	0.777
P$_{10}$	Hematite	8	10.5 mM	216	0.592	25.3	0.926
P$_{10}$	Goethite	8	10.5 mM	216	0.290	38.16	0.973
P$_{10}$	Lepidocrocite	8	10.5 mM	216	0.901	58.51	0.993

alkaline phosphatase was also found to decrease in ASW (Huang et al., 2018). The high salinity of seawater can lead to strong aggregation of metal (hydr)oxides (Keller et al., 2010), which may decrease effective surface area for polyphosphate adsorption and hydrolysis. Additionally, total P concentrations decreased at the beginning due to phosphate adsorption on Fe oxides, then gradually increased in the presence of lepidocrocite/hematite/goethite and decreased in the presence of ferrihydrite during 9-day hydrolysis (Fig. S9b).

P XANES results indicate that the main P species in ASW experiments are Fe oxide-adsorbed orthophosphate and polyphosphate and ACP solids (Fig. 7b-e), similar to the products of polyphosphate hydrolysis in the presence of 1 mM Ca^{2+} at pH 9 (Fig. 5). However, the percentages of ACP (11.4–22.5%) formed in ASW experiment is less than those (1.9–37.4% at pH 7.5 and 17.1–56% at pH 9) formed in experiments with 1 mM Ca^{2+} in DI water, despite of the higher concentration of total Ca^{2+} (10.5 mM) in ASW. Our recent studies found that both Mg^{2+} and Ca^{2+} can enhance the hydrolysis of polyphosphate on Al and Mn oxides in DI water and such enhancement increases with increasing concentrations of Ca^{2+} and Mg^{2+} (Wan et al., 2019a, b). The low content of ACP formed in ASW is possibly due to the increased aggregation of Fe oxides in ASW, which delays/prevents the hydrolysis and transformation of polyphosphate into ACP and subsequent transformation to crystalline apatite. The presence of high Mg^{2+} concentration (54.6 mM in ASW) might have also stabilized ACP via poisoning of crystal growth propagation for hydroxyapatite thus inhibiting the transformation of ACP to hydroxyapatite (Hilger et al., 2020).

4. DISCUSSION

Iron oxide surface contains μ-(hydr)oxo bridges that can complex with phosphate via bidentate binding (Kim et al., 2011; Huang, 2018). Previous studies showed that the coordination structure of phosphate groups on ferrihydrite, hematite, goethite, and lepidocrocite is dominantly binuclear bidentate (Elzinga and Sparks, 2007; Kim et al., 2011; Wang et al., 2013b; Wan et al., 2017b; Wang et al., 2017). This coordination structure is similar to that of organic phosphate complexation with metal cofactors (e.g., Mn, Fe, Zn, and Ca) in acid and alkaline phosphatase proteins (Rodriguez et al., 2014; Yong et al., 2014; Huang, 2018). Such structure makes the coordinated terminal phosphate moieties of polyphosphate prone to attack by proximal surface hydroxyl groups, and Fe oxides were thus

reported to mimic the behavior of phosphatase (Huang, 2018; Wan et al., 2019b). Ca^{2+} might perform as a chelating factor that enhances the adsorption density of polyphosphate on Fe oxides (Li et al., 2012) or as a metal cofactor that complexes with terminal phosphate groups (Yong et al., 2014). These two functions of Ca^{2+} can further increase the hydrolysis reactivity of Fe oxides for polyphosphate. Previous research on alkaline phosphatase showed that alkaline phosphatases have active sites containing one Fe(III) and two Ca(II) ions for *PhoD* phosphatase (Rodriguez et al., 2014) and two Fe(III) and three Ca(II) ions for *PhoX* phosphatase (Yong et al., 2014) (*PhoD* and *PhoX* are two common alkaline phosphatases in natural environments), and the water molecules bound to Ca(II) can be activated to catalyze the dephosphorylation of organic phosphate monoesters.

The maximum adsorption amounts of orthophosphate on 0.4 g L^{-1} Fe oxides is approximate 76–700 μM in the absence of Ca^{2+}, based on the reported adsorption density (2–3 μM m^{-2}) of Fe oxides (Wang et al., 2013a). Thus the total mass of Fe oxides in the suspension cannot provide enough surface to adsorb all phosphates including polyphosphate and the hydrolysis products (orthophosphate and shortened polyphosphate), which is further confirmed by the dynamics of total P concentration (Fig. S4). The competitive adsorption between unreacted/shorter-chained polyphosphate and orthophosphate is another key factor leading to the rapid hydrolysis of polyphosphate on Fe oxides due to more phosphate groups and higher negative charge of polyphosphate molecules. Thus polyphosphate can be viewed as a dissociation ligand to replace orthophosphate from surface reactive sites via competitive adsorption between the remained/shortened polyphosphate and the produced orthophosphate, which can further drive the continuous hydrolysis reaction of polyphosphate on Fe oxides.

The continuously produced orthophosphate can complex with Ca^{2+} to form ternary surface complexes and/or precipitates (Li et al., 2012; Wan et al., 2016), which decreases the concentrations of both Ca^{2+} and total P in the solution. For example, the complexation of orthophosphate with Ca to form calcium phosphate solids/minerals can drive the hydrolysis of polyphosphate via consuming the produced orthophosphate from the solution. We calculated the saturation state of the reaction solution using the software PHREEQC (Parkhurst and Appelo, 2013). The saturation indices with respect to hydroxyapatite in four Fe oxide systems after 9-day reaction are –3.97 to –3.08 for pH 6, 4.03–5.38 for pH 7.5, and 8.48–10.53 for pH 9. This suggests that the reaction suspensions are oversatu-
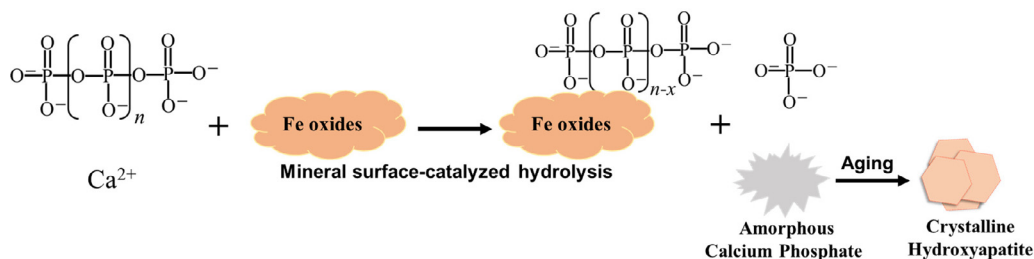
Fig. 8. Schematic illustration for the overall abiotic processes of polyphosphate hydrolysis and transformation into crystalline hydroxyapatite in the presence of Fe oxide minerals.

rated at pH 7.5 and 9, and are prone to the precipitation of calcium phosphate minerals. This is consistent with our P XANES results showing high percentages of ACP at these pH values (Fig. S8). For experiments conducted in ASW, the saturation indices for hydroxyapatite are 6.59–8.17, again suggesting the oversaturation for calcium phosphate minerals and can explain the observed ACP phase in the solid products (Fig. 5).

As polyphosphate hydrolysis and orthophosphate production further proceed, the precipitated ACP may gradually transform into crystalline calcium phosphate minerals upon long-term aging. A previous study indicated that the time frame for ACP transformation to crystalline calcium phosphate phases is dependent on solution chemistry (Eanes, 1998). High pH and temperature facilitate the transformation, whereas the presence of inorganic ions (e.g., Mg^{2+}, carbonate, and pyrophosphate) in ACP delays the transformation (Eanes, 1998). In our study, hydroxyapatite is the main crystalline calcium phosphate phase formed. Thus the primary pathway for polyphosphate transformation into crystalline hydroxyapatite in our system can be described by three major reactions (Fig. 8): (1) Fe oxides serves as abiotic catalysts (similar to phosphatase enzymes) to hydrolyze adsorbed polyphosphate via one-by-one cleavage of terminal P groups, which is enhanced in the presence of Ca^{2+}; (2) the produced orthophosphate complexes with Ca^{2+} to form ACP solids; (3) the formed ACP solids gradually transform into crystalline hydroxyapatite at room temperature and pressure.

The reactivity of Fe oxides for hydrolyzing polyphosphate relates to the surface area, surface structure, and exposed facet for phosphate complexation and hydrolysis. Ferrihydrite and hematite have higher surface areas than goethite, and both show higher apparent rates for polyphosphate hydrolysis. Lepidocrocite has layered structure and may have more reactive sites on the (100) and (001) planes that can catalyze polyphosphate rapid hydrolysis (Kim et al., 2011). Another possibility is related to the synthesis of lepidocrocite (which was based on the oxygenation of Fe(II) solution at neutral pH) that might lead to the potential presence of Fe(II) in the structure for enhanced polyphosphate hydrolysis. Due to the preferential precipitation of ACP solids at high pH values such as 7.5 and 9 (based on P K-edge XANES spectroscopy, Fig. 4), we mainly compare surface area normalized apparent hydrolysis rates of polyphosphate on four Fe oxides in the absence/presence of 1 mM Ca^{2+} at pH 6. The normalized apparent

hydrolysis rates follow the order of lepidocrocite $\approx$ goethite > hematite > ferrihydrite (Table 1). However, at pH 7.5 and 9, the order of the area-normalized apparent hydrolysis rate is lepidocrocite > goethite $\approx$ hematite > ferrihydrite. This implies that surface hydroxyls on Fe (oxyhydr)oxide minerals (lepidocrocite and goethite) may play an important role on catalyzing polyphosphate hydrolysis. A recent study indicated that the μ-(hydr)oxo Fe bridge structure in the Fe oxide nanoparticles was critical for the function of this natural metal oxides on catalyzing phosphate ester hydrolysis (Huang, 2018). The molecule scale mechanisms of polyphosphate hydrolysis on various Fe oxides and the differences in mineral phase and structure and surface hydroxyl populations are beyond the scope of this study and warrants future investigation.

Interfacial behaviors (adsorption, hydrolysis, and precipitation) of polyphosphate on environmentally abundant Fe oxides are of great relevance to understanding P cycling in aquatic environments. Our findings fill the knowledge gap between polyphosphate degradation and apatite formation, and help explain the rapid diagenesis of polyphosphate and P burial at sediment–water interface. Previous research showed that polyphosphate was a key intermediate for regulating the precipitation of fine-grained apatite and P burial at sediment–water interface, though the mechanisms were unclear and microbial activities were proposed to be a possible factor for polyphosphate transformation into crystalline apatite (Schulz and Schulz, 2005; Diaz et al., 2008; Goldhammer et al., 2010). This study shows that abiotic processes at the mineral-water interface could strongly mediate polyphosphate transformation, providing a new angle for explaining sedimentary P sequestration in geological environments. To our knowledge, this is the first study demonstrating the direct influences of natural minerals in controlling polyphosphate transformation into crystalline phosphate minerals. Future studies are warranted to explore polyphosphate transformation in different geological environments (e.g., freshwater vs seawater, presence of organic matter, sedimentary incubation) and molecular mechanisms (e.g., adsorption and hydrolysis) of polyphosphate on mineral surface, and further compare the relative or quantitative contributions of abiotic (e.g., mineral-catalyzed) vs biotic (e.g., enzymatic) processes in mediating polyphosphate hydrolysis and transformation, in order to further understand the processes influencing the transformation, fate, and bioavailability of complex phosphate-containing molecules in geological environments.

5. CONCLUSIONS

Four Fe oxides (i.e., ferrihydrite, hematite, goethite, and lepidocrocite) can strongly hydrolyze polyphosphate in the presence of Ca^{2+}, and the apparent hydrolysis rates follow the order of lepidocrocite > hematite > ferrihydrite > goethite. After normalization by specific surface area of Fe oxides, the hydrolysis rate is in the order of lepidocrocite ≈ goethite > hematite > ferrihydrite at pH 6, regardless of Ca^{2+} presence. At 7.5 and 9, the order of the area-normalized apparent hydrolysis rate is lepidocrocite > goethite ≈ hematite > ferrihydrite. A terminal-only pathway via one-by-one cleavage of terminal phosphate groups is proposed to be the dominant mechanism of mineral-catalyzed polyphosphate hydrolysis. Under alkaline pH conditions, polyphosphate hydrolysis leads to the precipitation of ACP in the presence of 1 mM Ca^{2+}, and the fraction of ACP increases as the pH value increases. The newly formed ACP eventually transforms to crystalline hydroxyapatite upon long-term aging of 70 or 150 days. The hydrolysis rate of polyphosphate and the percentage of ACP formed are relatively low in ASW, due to its high ionic strength and the high concentration of Mg^{2+}.

Declaration of Competing Interest

The authors declare that they have no known competing financial interests or personal relationships that could have appeared to influence the work reported in this paper.

APPENDIX A. SUPPLEMENTARY DATA

Supplementary data to this article can be found online at https://doi.org/10.1016/j.gca.2021.04.031.

REFERENCES

Abdala D. B., Northrup P. A., Arai Y. and Sparks D. L. (2015a) Surface loading effects on orthophosphate surface complexation at the goethite/water interface as examined by extended X-ray Absorption Fine Structure (EXAFS) spectroscopy. *J. Colloid Interface Sci.* **437**, 297–303.

Abdala D. B., Northrup P. A., Vicentin F. C. and Sparks D. L. (2015b) Residence time and pH effects on the bonding configuration of orthophosphate surface complexes at the goethite/water interface as examined by Extended X-ray Absorption Fine Structure (EXAFS) spectroscopy. *J. Colloid Interface Sci.* **442**, 15–21.

Alexandratos V. G., Behrends T. and Van Cappellen P. (2017) Fate of adsorbed U(VI) during sulfidization of lepidocrocite and hematite. *Environ. Sci. Tech.* **51**, 2140–2150.

ASTM D1141-98, (2013). Standard for the Preparation of Substitute Ocean Water. 2013. ASTM International, West Conshohocken, PA.

Brandes J. A., Ingall E. and Paterson D. (2007) Characterization of minerals and organic phosphorus species in marine sediments using soft X-ray fluorescence spectromicroscopy. *Mar. Chem.* **103**, 250–265.

Cabrol L., Quéméneur M. and Misson B. (2017) Inhibitory effects of sodium azide on microbial growth in experimental resuspension of marine sediment. *J. Microbiol. Meth.* **133**, 62–65.

Cornell R. M. and Schwertmann U. (2004) The Iron Oxides. *Wiley-VCH Verlag GmbH & Co. KGaA*, 553–646.

Das P., Metcalfe C. D. and Xenopoulos M. A. (2014) Interactive effects of silver nanoparticles and phosphorus on phytoplankton growth in natural waters. *Environ. Sci. Tech.* **48**, 4573–4580.

Davantès A., Costa D. and Lefèvre G. (2016) Molybdenum(VI) adsorption onto lepidocrocite (γ-FeOOH): *In situ* vibrational spectroscopy and DFT+U theoretical study. *J. Phys. Chem. C* **120**, 11871–11881.

Diaz J., Ingall E., Benitez-Nelson C., Paterson D., de Jonge M. D., McNulty I. and Brandes J. A. (2008) Marine polyphosphate: A key player in geologic phosphorus sequestration. *Science* **320**, 652–655.

Diaz J. M. and Ingall E. D. (2010) Fluorometric quantification of natural inorganic polyphosphate. *Environ. Sci. Tech.* **44**, 4665–4671.

Diaz J. M., Ingall E. D., Snow S. D., Benitez-Nelson C. R., Taillefert M. and Brandes J. A. (2012) *Potential role of inorganic polyphosphate in the cycling of phosphorus within the hypoxic water column of Effingham Inlet*. British Columbia. Global Biogeochem, Cy, p. 26.

Eanes E. D. (1998) Amorphous Calcium Phosphate: Thermodynamic and Kinetic Considerations. In *Calcium Phosphates in Biological and Industrial Systems* (ed. Z. Amjad). Springer, US, Boston, MA, pp. 21–39.

Ebuele V. O., Santoro A. and Thoss V. (2016) Phosphorus speciation by ^{31}P NMR spectroscopy in bracken (*Pteridium aquilinum* (L.) Kuhn) and bluebell (*Hyacinthoides non-scripta* (L.) Chouard ex Rothm.) dominated semi-natural upland soil. *Sci. Total Environ.* **566–567**, 1318–1328.

Elzinga E. J. and Sparks D. L. (2007) Phosphate adsorption onto hematite: An *in situ* ATR-FTIR investigation of the effects of pH and loading level on the mode of phosphate surface complexation. *J. Colloid Interface Sci.* **308**, 53–70.

Fang W., Sheng G. P., Wang L. F., Ye X. D. and Yu H. Q. (2015) Quantitative evaluation of noncovalent interactions between polyphosphate and dissolved humic acids in aqueous conditions. *Environ. Pollut.* **207**, 123–129.

Fang Y., Kim E. and Strathmann T. J. (2018) Mineral- and base-catalyzed hydrolysis of organophosphate flame retardants: Potential major fate-controlling sink in soil and aquatic environments. *Environ. Sci. Tech.* **52**, 1997–2006.

Franke R. and Hormes J. (1995) The P K-near edge absorption spectra of phosphates. *Physica B* **216**, 85–95.

Goldhammer T., Bruchert V., Ferdelman T. G. and Zabel M. (2010) Microbial sequestration of phosphorus in anoxic upwelling sediments. *Nat. Geosci.* **3**, 557–561.

Guan X.-H., Liu Q., Chen G.-H. and Shang C. (2005) Surface complexation of condensed phosphate to aluminum hydroxide: An ATR-FTIR spectroscopic investigation. *J. Colloid Interface Sci.* **289**, 319–327.

Guo H. and Barnard A. S. (2013) Naturally occurring iron oxide nanoparticles: Morphology, surface chemistry and environmental stability. *J Mater Chem A* **1**, 27–42.

Hamilton J. G., Hilger D. and Peak D. (2017) Mechanisms of tripolyphosphate adsorption and hydrolysis on goethite. *J. Colloid Interface Sci.* **491**, 190–198.

Hilger D. M., Hamilton J. G. and Peak D. (2020) The Influences of magnesium upon calcium phosphate mineral formation and structure as monitored by X-ray and vibrational spectroscopy. *Soil Syst.* **4**, 8.

Huang R. and Tang Y. (2016) Evolution of phosphorus complexation and mineralogy during (hydro)thermal treatments of activated and anaerobically digested sludge: Insights from sequential extraction and P K-edge XANES. *Water Res.* **100**, 439–447.

Huang R., Wan B., Hultz, M. Diaz J.M. and Tang Y. (2018) Phosphatase-mediated hydrolysis of linear polyphosphates. Environ. Sci. Tech. 52, 1183-1190.

Huang R. X. and Tang Y. Z. (2015) Speciation dynamics of phosphorus during (hydro)thermal treatments of sewage sludge. *Environ. Sci. Tech.* **49**, 14466–14474.

Huang X.-L. (2018) Hydrolysis of phosphate esters catalyzed by inorganic iron oxide nanoparticles acting as biocatalysts. *Astrobiology* **18**, 294–310.

Hupfer M., Ruübe B. and Schmieder P. (2004) Origin and diagenesis of polyphosphate in lake sediments: A ^{31}P-NMR study. *Limnol. Oceanogr.* **49**, 1–10.

Inman M. P., Beattie J. K., Jones D. R. and Baldwin D. S. (2001) Abiotic hydrolysis of the detergent builder tripolyphosphate by hydrous manganese dioxide. *Water Res.* **35**, 1987–1993.

Keller A. A., Wang H., Zhou D., Lenihan H. S., Cherr G., Cardinale B. J., Miller R. and Ji Z. (2010) Stability and aggregation of metal oxide nanoparticles in natural aqueous matrices. *Environ. Sci. Tech.* **44**, 1962–1967.

Khare N., Hesterberg D. and Martin J. D. (2005) XANES investigation of phosphate sorption in single and binary systems of iron and aluminum oxide minerals. *Environ. Sci. Tech.* **39**, 2152–2160.

Kim J., Li W., Philips B. L. and Grey C. P. (2011) Phosphate adsorption on the iron oxyhydroxides goethite (α-FeOOH), akaganeite (β-FeOOH), and lepidocrocite (γ-FeOOH): A ^{31}P NMR study. *Energ. Environ. Sci.* **4**, 4298–4305.

Kornberg A., Rao N. N. and Ault-Riche D. (1999) Inorganic polyphosphate: A molecule of many functions. *Annu. Rev. Biochem.* **68**, 89–125.

Kulakovskaya T. V., Vagabov V. M. and Kulaev I. S. (2012) Inorganic polyphosphate in industry, agriculture and medicine: Modern state and outlook. *Process Biochem.* **47**, 1–10.

Lanzl C. A., Baltrusaitis J. and Cwiertny D. M. (2012) Dissolution of hematite nanoparticle aggregates: Influence of primary particle size, dissolution mechanism, and solution pH. *Langmuir* **28**, 15797–15808.

Li W., Xu W., Parise J. B. and Phillips B. L. (2012) Formation of hydroxylapatite from co-sorption of phosphate and calcium by boehmite. *Geochim. Cosmochim. Acta* **85**, 289–301.

Majed N., Matthäus C., Diem M. and Gu A. Z. (2009) Evaluation of intracellular polyphosphate dynamics in enhanced biological phosphorus removal process using Raman microscopy. *Environ. Sci. Tech.* **43**, 5436–5442.

Martin P., Dyhrman S. T., Lomas M. W., Poulton N. J. and Van Mooy B. A. S. (2014) Accumulation and enhanced cycling of polyphosphate by Sargasso Sea plankton in response to low phosphorus. *Proc. Natl. Acad. Sci. U.S.A.* **111**, 8089–8094.

McDowell R. W. and Stewart I. (2005) Peak assignments for phosphorus-31 nuclear magnetic resonance spectroscopy in pH range 5–13 and their application in environmental samples. *Chem. Ecol.* **21**, 211–226.

Michelmore A., Gong W., Jenkins P. and Ralston J. (2000) The interaction of linear polyphosphates with titanium dioxide surfaces. *Phys. Chem. Chem. Phys.* **2**, 2985–2992.

Murphy J. and Riley J. P. (1962) A modified single solution method for the determination of phosphate in natural waters. *Anal. Chim. Acta* **27**, 31–36.

Nguyen Dang D., Gascoin S., Zanibellato A., G. Da Silva C., Lemoine M., Riffault B., Sabot R., Jeannin M., Chateigner D. and Gil O. (2017) Role of brucite dissolution in calcium carbonate precipitation from artificial and natural seawaters. Cryst. Growth Des. 17, 1502-1513.

Omelon S. J. and Grynpas M. D. (2008) Relationships between polyphosphate chemistry, biochemistry and apatite biomineralization. *Chem. Rev.* **108**, 4694–4715.

Orchard E. D., Benitez-Nelson C. R., Pellechia P. J., Lomas M. W. and Dyhrman S. T. (2010) Polyphosphate in *Trichodesmium* from the low-phosphorus Sargasso Sea. *Limnol. Oceanogr.* **55**, 2161–2169.

Parkhurst D. L. and Appelo C. A. J. (2013) *Description of input and examples for PHREEQC version 3: A computer program for speciation, batch-reaction, one-dimensional transport, and inverse geochemical calculations*. VA, Techniques and Methods, Reston, p. 519.

Paytan A., Cade-Menun B. J., McLaughlin K. and Faul K. L. (2003) Selective phosphorus regeneration of sinking marine particles: Evidence from ^{31}P-NMR. *Mar. Chem.* **82**, 55–70.

Paytan A. and McLaughlin K. (2007) The oceanic phosphorus cycle. *Chem. Rev.* **107**, 563–576.

Rao N. N., Gómez-García M. R. and Kornberg A. (2009) Inorganic polyphosphate: Essential for growth and survival. *Annu. Rev. Biochem.* **78**, 605–647.

Ravel B. and Newville M. (2005) ATHENA, ARTEMIS, HEPHAESTUS: Data analysis for X-ray absorption spectroscopy using IFEFFIT. *J. Synchrotron Radiat.* **12**, 537–541.

Rodriguez F., Lillington J., Johnson S., Timmel C. R., Lea S. M. and Berks B. C. (2014) Crystal structure of the bacillus subtilis phosphodiesterase PhoD reveals an iron and calcium-containing active site. *J. Biol. Chem.* **289**, 30889–30899.

Sannigrahi P. and Ingall E. (2005) Polyphosphates as a source of enhanced P fluxes in marine sediments overlain by anoxic waters: Evidence from ^{31}P NMR. *Geochem. Trans.* **6**, 52–59.

Schulz H. N. and Schulz H. D. (2005) Large sulfur bacteria and the formation of phosphorite. *Science* **307**, 416–418.

Skipper H. D. and Westermann D. T. (1973) Comparative effects of propylene oxide, sodium azide, and autoclaving on selected soil properties. *Soil Biol. Biochem.* **5**, 409–414.

Skrtic D., Antonucci J. M., Eanes E. D. and Brunworth R. T. (2002) Silica- and zirconia-hybridized amorphous calcium phosphate: Effect on transformation to hydroxyapatite. *J. Biomed. Materi. Res.* **59**, 597–604.

Wan B., Huang R., Diaz J. M. and Tang Y. (2019a) Manganese oxide catalyzed hydrolysis of polyphosphates. *ACS Earth Space Chem.* **3**, 2623–2634.

Wan B., Huang R., Diaz J. M. and Tang Y. (2019b) Polyphosphate adsorption and hydrolysis on aluminum oxides. *Environ. Sci. Tech.* **53**, 9542–9552.

Wan B., Yan Y., Liu F., Tan W., Chen X. and Feng X. (2016) Surface adsorption and precipitation of inositol hexakisphosphate on calcite: A comparison with orthophosphate. *Chem. Geol.* **421**, 103–111.

Wan B., Yan Y., Tang Y., Bai Y., Liu F., Tan W., Huang Q. and Feng X. (2017a) Effects of polyphosphates and orthophosphate on the dissolution and transformation of ZnO nanoparticles. *Chemosphere* **176**, 255–265.

Wan B., Yan Y. P., Zhu M. Q., Wang X. M., Liu F., Tan W. F. and Feng X. H. (2017b) Quantitative and spectroscopic investigations of the co-sorption of *myo*-inositol hexakisphosphate and cadmium(II) on to haematite. *Eur. J. Soil Sci.* **68**, 374–383.

Wang X., Liu F., Tan W., Li W., Feng X. and Sparks D. L. (2013a) Characteristics of phosphate adsorption-desorption onto ferrihydrite: Comparison with well-crystalline Fe (hydr)oxides. *Soil Sci.* **178**, 1–11.

Wang X., Hu Y., Tang Y., Yang P., Feng X., Xu W. and Zhu M. (2017) Phosphate and phytate adsorption and precipitation on ferrihydrite surfaces. *Environ. Sci. Nano* **4**, 2193–2204.

Wang X., Li W., Harrington R., Liu F., Parise J. B., Feng X. and Sparks D. L. (2013b) Effect of ferrihydrite crystallite size on phosphate adsorption reactivity. *Environ. Sci. Tech.* **47**, 10322–10331.

Yong S. C., Roversi P., Lillington J., Rodriguez F., Krehenbrink M., Zeldin O. B., Garman E. F., Lea S. M. and Berks B. C. (2014) A complex iron-calcium cofactor catalyzing phosphotransfer chemistry. *Science* **345**, 1170.

Yuan W., Zhou Y., Liu X. and Wang J. (2019) New perspective on the nanoplastics disrupting the reproduction of an endangered fern in artificial freshwater. *Environ. Sci. Tech.* **53**, 12715–12724.

Zhang F., Blasiak L. C., Karolin J. O., Powell R. J., Geddes C. D. and Hill R. T. (2015) Phosphorus sequestration in the form of polyphosphate by microbial symbionts in marine sponges. *Proc. Natl. Acad. Sci. U.S.A.* **112**, 4381–4386.

Associate editor: Jean-francois Boily